Numerical simulation of fracture mode transition in ductile plates

Liang Xue *, Tomasz Wierzbicki

Department of Mechanical Engineering, Massachusetts Institute of Technology, 77 Massachusetts Avenue 5-218, Cambridge, MA 02139, USA

ARTICLE INFO

ABSTRACT

Fracture mode of ductile solids can vary depending on the history of stress state the material experienced. For example, ductile plates under remote in-plane loading are often found to rupture in mode I or mixed mode I/III. The distinct crack patterns are observed in many different metals and alloys, but until now the underlying physical principles, though highly debated, remain unresolved. Here we show that the existing theories are not capable of capturing the mixed mode I/III due to a missing ingredient in the constitutive equations. We introduce an azimuthal dependent fracture envelope and illustrate that two competing fracture mechanisms, governed by the pressure and the Lode angle of the stress tensor, respectively, exist ahead of the crack tip. Using the continuum damage plasticity model, we demonstrate that the distinctive features of the two crack propagation modes in ductile plates can be reproduced using three dimensional finite element simulations. The magnitude of the tunneling effect and the apparent crack growth resistance are calculated and agree with experimental observations. The finite element mesh size dependences of the fracture mode and the apparent crack growth resistance are also investigated.

Published by Elsevier Ltd.

1. Introduction

A thorough physical understanding of ductile crack initiation and propagation is of essential interest to many scientific disciplines and engineering applications. Existing constitutive models are so far not capable of predicting and explaining several key features of ductile fracture known to experimentalists, such as the flat to slant transition of fracture modes in flat ductile panels. Mathematical simplification has been given to macrocracks in solids such that a singularity is placed at the crack tip in the scope of conventional fracture mechanics. The treatment for crack advance is described by field variables remote to the crack tip such that the singularity no longer poses problems. This treatment works for brittle and quasi-brittle materials where the fracture process zone is small compared with the specimen geometries and the specimen dimensions are large enough to assess field variables away from the crack tip. In reality, however, these assumptions do not hold for the many metallic materials where large plastic deformation precedes the occurrence of fracture. Crack blunting and necking greatly reduce the accuracy of these simplifications and idealizations. Moreover, the geometry of the solid bodies is often too complex to calculate and the cracked body may not be idealized as plane strain condition, such that theoretical solutions exist

(Hutchinson, 1968; Rice and Rosengren, 1968), due to the constraint length scale in practical problems. These issues cannot be resolved without considering the details about the crack process zone ahead of a ductile crack.

Traditionally, the plane strain models near the crack tip is used in finite element analyses using explicitly modeled voids in the crack path (e.g. Gao et al., 2006; Kim et al., 2007; Xia et al., 1995). We show here that, with an additional dimension in the continuum damage plasticity theory, experimentally observed ductile crack patterns and trends in the crack growth resistance can be predicted using three dimensional finite element simulations. In a laboratory setup, pre-cracked flat plates are often used to study ductile crack propagation. Although some materials show a continuation of a flat mode I crack (which is normal to the plate surface and to the remotely applied load), a transition from a flat pre-crack to a slant mixed mode I/III crack (which is approximately 45° to the surface) in thin plates is commonly observed in experiments for many polycrystalline metals and alloys (Anderson, 2005; Barsom and Rolfe, 1999; Broek, 1982; Knott, 1973). Fractographically, a mode I flat fracture surface is of a fibrous nature and a slant mixed mode I/III fracture surface is a shear type of failure and is less voided compared with a flat crack surface (Barsom and Rolfe, 1999; Benzerga et al., 2004; Cottrell, 1965; Pineau and Pardoen, 2007; Thomason, 1990). However, why and how this transition of the global fracture mode occurs is not fully understood. The vast experimental slant fracture results (e.g. Dawicke and Sutton, 1994; Irwin et al., 1958; Mahmoud and Lease, 2003; Newman, 1985; Srawley and Brown, 1965) are in sharp contrast with the absence

* Corresponding author. Present address: Department of Mechanical Engineering, Northwestern University, 2145 Sheridan Road, M-110, Evanston, IL 60208, USA. Tel.: +1 847 467 2435.

E-mail address: xue@alum.mit.edu (L. Xue).

of slant crack predicted by three dimensional finite element analyses using existing constitutive theories (e.g. Roy and Dodds, 2001; Dawicke et al., 1995; Gullerud et al., 1999; James and Newman, 2003; Lan et al., 2006; Li et al., 2002; Mahmoud and Lease, 2004; Newman et al., 2003; Tvergaard and Needleman, 2006). This discrepancy between theories and experiments is resolved here through a new isotropic continuum damage plasticity theory, which adopts a scalar measurement of damage from a three dimensional description.

We begin with the experimentally observed differences between the flat and slant modes in cracked plates. The slant region of fracture is not a mode III crack but involves some pulling apart (mode I). Besides the apparent fracture angle to surface, there are several generally perceived distinctive features and trends between the two aforementioned ductile crack modes, as shown in Fig. 1. These features and trends include: (i) A flat crack is usually observed for strong strain hardenable materials; and a slant crack is usually observed for low strain hardenable materials. (ii) Significant necking often precedes the appearance of a ductile flat crack; while there is often very little neck ahead of a slant crack tip. (iii) A flat crack front shows significant tunneling in the mid plane; while a slant crack front shows little tunneling throughout the thickness. (iv) Flat cracks are usually found for thicker plates (although shear lips may exist near surface); and slant cracks are more often found for thinner plates. (v) Materials are found to exhibit flat cracks at a quasi-static loading rate may change to a slant crack upon dynamic loading (see Rivalin et al., 2001). These features will be replicated here by a series of numerical simulations.

Here we show how mode transition is controlled by the interaction of the pressure and the azimuthal angle of the stress states which dominate the damage accumulation in the plastic process zone ahead of the crack tip by extensive finite element simulations. The azimuthal dependence on an octahedral plane for ductile fracture is found to be a missing ingredient that is responsible for the fracture mode transition. We demonstrate using compact tension specimen that mode transition is determined by the combination of strain hardening capability, the azimuthal dependence and the pressure sensitivity of the fracture characteristics of the material. In the crack process zone, the mode of crack is determined by two competing mechanisms: (i) a flat pattern dominated by the pressure effect with tunneling that can be captured by existing damage theories; (ii) a slant crack about 45° to the surface driven by the azimuthal (the Lode angle) dependence of ductile fracture, which de facto is the controlling factor of mixed mode I/III for thin plates. This Lode angle dependence introduces the effect of the third invariant J_3 of the stress tensor. Our results demonstrate that the azimuthal dependence of ductile fracture together with the pressure sensitivity plays a vital role in determining the fracture pattern. We anticipate the present study to lead to more accurate modeling of ductile fracture at a continuum length scale. For example, crack predictions in metal forming and failure analyses of large scale structures.

2. Continuum theory of damage plasticity

Stripped to its essentials, the continuum damage plasticity model consists of (1) a classical strain hardening and associated flow rule for the plasticity of the matrix material; (2) an evolution law for the ductile damage to depict the microstructural rearrangement along the plastic loading path; and (3) a damage coupled yield condition to account for the material deterioration due to the microstructural change. For simplicity, we employ von Mises yield criterion for the matrix which only depends on the second invariant of the stress deviator. The evolution law of ductile damage described by a three dimensional "cylindrical decomposition" (Xue, 2007a), which incorporates all three stress invariants, i.e. I_1, J_2 and J_3. The evolution of damage resembles the evolution of equivalent stress in conventional plasticity theories. Here, we summarize this damage model below.

Because the plastic damage is path dependent, the damage is given in the rate form, which relies on the concept of fracture envelope. A fracture envelope is defined in the three dimensional space of the triaxial plastic strain plane and the hydrostatic pressure. The fracture envelope is characterized by the plastic strains at which material fracture occurs from all possible loading paths of constant pressure and constant azimuthal angle. The pressure sensitivity and the azimuthal dependence of the fracture strains are described by a pressure dependence function $\mu_p(p)$ and an azimuthal dependence function $\mu_\theta(\theta_L)$, respectively.

An illustrative fracture envelope for a ductile material is sketched in Fig. 2. The vertical axis is the mean stress (i.e. negative pressure) and the triaxial horizontal plane is the principal plastic strain plane, which characterizes the azimuthal angle on an octahedral plane when the plastic deformation is assumed to be isochoric. Many materials, such as rocks and metals, exhibit higher ductility under high compressive pressure. This phenomenon has been extensively studied in the past century (e.g. see monographs by Bridgman (1952) and Pugh (1970)). In the present model, the azimuthal dependence of the fracture envelope is described by six peaks (at generalized tension and compression conditions) and six valleys (at generalized shear conditions). In other words, ductile fracture of solids is more sensitive to shear type of loading. This consideration is based on the observation of many experiment results (see e.g. Bao and Wierzbicki, 2004; Barsoum and Faleskog, 2007; Clausing, 1970; McClintock, 1971; Wilkins et al., 1980). It should be noted that convexity does not apply to fracture envelope,
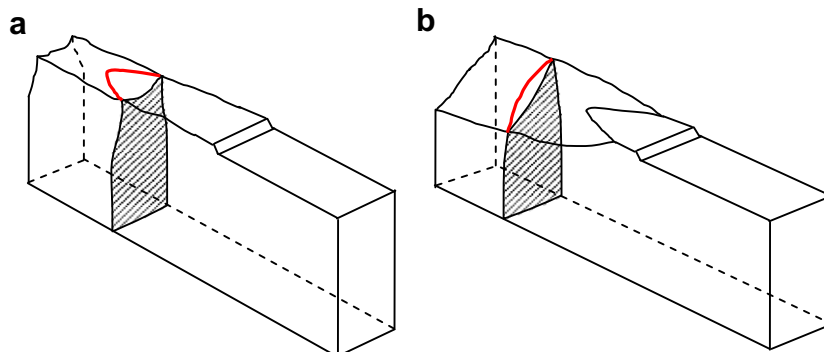
a   **b**

Fig. 1. The two distinct modes of crack in ductile plates (a) flat mode; (b) slant mode. Shaded areas are the cross-sections perpendicular to the crack propagation direction. Red lines indicate the crack fronts. (For interpretation of the references to color in this figure legend, the reader is referred to the web version of this paper.)
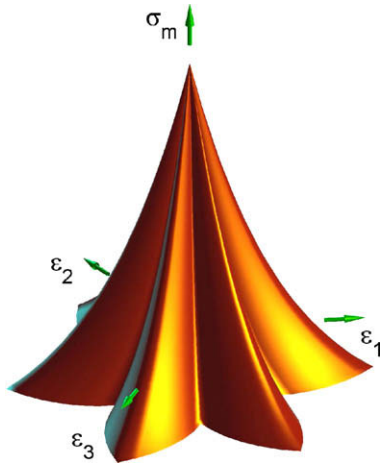
Fig. 2. A three-dimensional representation of the fracture envelope in the space of the principal plastic strains (ε_1, ε_2 and ε_3) and the mean stress σ_m.

since it is a collection fracture strains from prescribed loading paths and is based on measurement of strains rather than stresses. For isotropic materials, the azimuthal angle can be characterized by the Lode angle, which varies from $-\pi/6$ to $\pi/6$ and is defined for each sextant of the octahedral plane. Here, we restrict ourselves to isotropic materials such that the fracture envelope is periodic, i.e. it is identical in each of these six sextants.

We start by separating the matrix material, which is defect free, from the macroscopic structure of solid. The weakening effect due to the deterioration of the material is introduced by the damage-coupled yield condition:

$$\Phi = \sigma_{eq} - w(D)\sigma_M \leqslant 0. \tag{1}$$

For arbitrary plastic loading path, the damage is calculated by the following integral:

$$D = \int_0^{\varepsilon_c} m\left(\frac{\varepsilon_p}{\varepsilon_f}\right)^{(m-1)} \frac{d\varepsilon_p}{\varepsilon_f} \leqslant 1, \tag{2}$$

where m is a material parameter, ε_f is a fracture strain envelope defined on the stress state and ε_c is the critical strain at which fracture occurs. It is assumed $D = 0$ for virgin material and $D = 1$ for a complete loss of load carrying capacity, i.e. fracture occurs. It can be verified that for loading paths with constant fracture strain ε_f the above definite integration reaches unity when $\varepsilon_c = \varepsilon_f$.

We assume the Young's modulus of the material decrease as damage accumulates, i.e. $E(D) = w(D)E_0$, where E_0 is the original undamaged Young's modulus. The weakening function $w(D)$ in Eq. (1) is described by

$$w(D) = 1 - D^\beta, \tag{3}$$

where β is a material constant to be calibrated from fitting experimental curves.

The fracture strain envelope is defined on the current pressure and the Lode angle θ_L only

$$\varepsilon_f(p, \theta_L) = \varepsilon_{f0}\mu_p(p)\mu_\theta(\theta_L), \tag{4}$$

where ε_{f0} is a material constant and $\mu_p(p)$ and are $\mu_\theta(\theta_L)$ the pressure sensitivity function and the azimuthal angle dependence function, which in the present study adopt a logarithmic form of pressure dependence function:

$$\mu_p(p) = \begin{cases} 1 - q\log\left(1 - \frac{p}{p_{lim}}\right), & p \geqslant p_{lim}[1 - \exp(1/q)]; \\ 0, & p < p_{lim}[1 - \exp(1/q)], \end{cases} \tag{5}$$

and the second kind of Lode angle dependence function:

$$\mu_\theta(\theta_L) = \gamma + (1 - \gamma)\left(\frac{6|\theta_L|}{\pi}\right)^k, \tag{6}$$

where q, p_{lim}, γ and k are material constants, p is the current pressure and θ_L is the Lode angle ($\theta_L \in [-\pi/6, \pi/6]$). The Lode angle is one of several parameters that are commonly used to denote the azimuthal angle on an octahedral plane in the principal stress space. The Lode angle is defined by the principal stress components

$$\theta_L = \tan^{-1}\left(\frac{1}{\sqrt{3}}\frac{2\sigma_2 - \sigma_1 - \sigma_3}{\sigma_1 - \sigma_3}\right) \quad \text{or}$$

$$\theta_L = -\frac{1}{3}\sin^{-1}\left(\frac{27}{2}\frac{J_3}{\sigma_{eq}^3}\right), \tag{7}$$

where σ_1, σ_2 and σ_3 are the ordered principal stress components and $J_3 = s_1s_2s_3$ is the third stress invariant where s_1, s_2 and s_3 are the ordered principal stress deviator components.

In this set of constitutive equations, six material parameters are used in total. These material parameters are a reference strain ε_{f0}, two for pressure dependence function p_{lim}, q, two for the Lode angle dependence function γ and k, one for the damage accumulation exponent m and one for the weakening effect β. These parameters are treated as constants for a given material and are to be calibrated from experiments. Xue and Wierzbicki (submitted for publication) presented a combined experimental and numerical procedure to calibrate aluminum alloy 2024-T351 using a series of tests at different mean stresses and Lode angles.

To summarize the above method, a nonlinear integral for damage is adopted (Eq. (2)). In Eq. (2), the integrand, i.e. the accumulation rate of damage (a non-negative value), is implicitly influenced by the pressure and the Lode angle of the current stress state by the respective effects on the fracture envelope ε_f for a given incremental plastic strain $\dot{\varepsilon}_p$. The weakening effect of the accumulated damage enters the yield condition through a weakening factor $w(D)$, which depends on the magnitude of damage at the current state. The strain hardening effect enters the yield condition through the matrix stress–strain relationship σ_M, which is a function of the equivalent plastic strain. The stress integration procedure for explicit algorithm is summarized in Appendix A.

In a previous paper, Xue and Wierzbicki (2008) adopted the present theory and found that the synergistic combination of the Lode angle dependence and the weakening factor governs a slant mode in compact tension specimens and promotes shear lips. In the present paper, we further explore the transition of fracture mode on various material and geometry aspects of the compact tension tests. These factors include the Lode angle sensitivity parameter, the strain hardening, the pressure sensitivity and the thickness of the compact tension plate. Their effects on the fracture mode, the tunneling of crack front and the apparent crack growth resistance, R, are discussed.

3. Modeling

We consider a base scenario of a compact tension specimen according to ASME E399 with width $W = 50.8$ mm, thickness $B = 6.35$ mm, a pre-crack of $60°$ notch angle (normal to surface) and a crack to width ratio $a/W = 0.5$. The external load is applied in the two cylindrical holes through pulling apart of two frictionless pins inside the holes in a single stroke. No fatigue crack is considered.

In Sections 4–6, the compact tension specimen is discretized into 145,400 8-node reduced integration elements. Twenty elements are used in the thickness direction and the aspect ratio of the elements along the crack path is about 1:1:1. The element size in central zone where the crack path is anticipated is approximately 0.3 mm × 0.3 mm × 0.3 mm ($W \times L \times H$). Same mesh size are used in Section 7 for the thickness dependence simulations,

where additional elements are added in the thickness direction. In Section 8, the base scenario compact tension specimen is adopted for the mesh size dependence simulations, where element size is varied. All simulations are carried out using LS-DYNA with the damage plasticity model implemented as a user subroutine. The stress integration procedure is included in Appendix A.

The matrix stress–strain relationship is assumed to follow the Swift type of power law relationship

$$\sigma_M = \sigma_{y0}(1 + \varepsilon_p/\varepsilon_0)^n, \tag{8}$$

where σ_{y0} is the initial yield stress of the matrix, n is the hardening exponent, ε_0 is a reference strain, ε_p is the plastic strain and σ_M is the equivalent matrix stress.

In the present study, we focus on the dependence of fracture modes and crack growth resistance on the strain hardening, the Lode angle dependence and pressure sensitivity. In order to draw conclusions from these influencing factors, we adopt the following set of fixed parameters in the numerical study Young's modulus $E = 70$ GPa, Poisson's ration $v = 0.3$, mass density $\rho = 2700$ kg/m³, $\sigma_{y0} = 300$ MPa, $\varepsilon_0 = 0.008$, $\varepsilon_{f0} = 0.8$, $p_{lim} = 1000$ MPa, $k = 1.0$, $m = 2.0$, $\beta = 2.0$ and n, q and γ will be varied to perform a parametric study. The choice of fixed parameters is based on an aluminum alloy tested and calibrated for the damage plasticity model (Xue, 2007b; Xue and Wierzbicki, submitted for publication).

4. Effect of azimuthal dependence

In this section, studied is the dependence of the crack propagation patterns on the material parameters of γ. Material constants $n = 0.2$, $q = 1.0$ are chosen for this example. The mixed mode I/III and mode I of cracks are shown in Fig. 3. Fig. 3(a) shows a transition from a flat starting crack with tunneling to a slant crack throughout the thickness direction for $\gamma = 0.5$. Fig. 3(b) shows continuing flat crack propagation in the entire thickness for $\gamma = 0.7$. The difference in the azimuthal sensitivity of the fracture envelope triggers the change in the crack mode. With diminishing azimuthal dependence of ductile fracture ($\gamma \to 1.0$), the compact tension crack changes from a slant crack to a flat one. This is consistent with the result in Xue and Wierzbicki (2008) that shows a slant crack can only be predicted for materials with both effects of the azimuthal angle dependence and the weakening of material strength. Fig. 4 shows a comparison of the two different modes while propagating along the ligament. Note the differences in the crack fronts, where propagating flat crack shows a more significant tunnel in the mid section. A fully developed slant crack is relatively straight compared with a parabolic curved flat crack front.

The extent of necking in the path of the stable crack propagation is indicated by the distance from the fracture edge to the edges of the undeformed plate which are indicated by the horizontal thin lines in Fig. 4. In these simulation results, the shrinkage in the thickness direction at the vicinity of crack is more severe for the mode I case than the mixed mode I/III case. This agrees with feature (ii) of experimental observations.

The load versus load line displacement and the normalized tunneling versus mid-plane crack extension for various γ values are plotted in Fig. 5(a) and (b). For a straight pre-cracked flat plate, the fracture starts at the mid-plane and propagates both forward and laterally to the surface. The crack front is usually a parabolic shape, and is thus often called "tunneling". The extent of tunneling is defined as the difference of crack extension at mid-plane and at surface divided by the original plate thickness (Dawicke and Sutton, 1994). For mode I, the tunneling remains at a high level after initial crack forms over the entire thickness. However, for slant crack propagation, the tunneling drops sharply after a maximum value is reached. This distinct feature of tunneling is identified in Fig. 5(b) and (c) as the shape of tunneling evolution curves can be categorized into two groups depending on the γ values. The simulation results agree with experimentally observed feature (iii).

The mode transition from slant to flat mode occurs at about $\gamma = 0.65$ in this case. There exists a steep transition of average tunneling between the two full fledged propagation modes (as shown in Fig. 5(c)). On the left-hand-side of the mode transition line, slant cracks develop and the stable normalized tunneling increases with increasing γ. On the right-hand-side of the mode transition line, flat cracks appear and the stable normalized tunneling decreases with increasing γ, which indicates the mid-plane crack extension is increasingly longer than the crack extension at the surface for decreasing γ values. The advance of mid-plane crack is understood as the mid-plane material is subjected to more severe plane strain condition than the surface materials; therefore, the mid-plane material is more prone to fracture for lower γ values. However, such advances in the mid-plane are not sustainable as the material parameter γ drops further. A global mode transition occurs when the crack finds itself an easy path to propagate divergently to surfaces at an approximately 45° angle. Consequently, shear lips form at the tail of the crack near surfaces. The shear lips grow and eventually merge to form a slant crack over the entire thickness. When opposite shear lips form, a small portion of anti-symmetric load is introduces to the nominally symmetric loading system. This can be seen in Fig. 4 as the remote edges of a slant cracked specimen (horizontal thin lines) are no longer overlapping, which further promotes a mixed mode I/III to form. For a flat cracked specimen, the loading system remains symmetric with respect to the mid-plane; therefore, the remote edges remain overlapping (Fig. 4(a)).

It is also noted that the apparent crack growth resistance is found to be a strong function of the material parameter
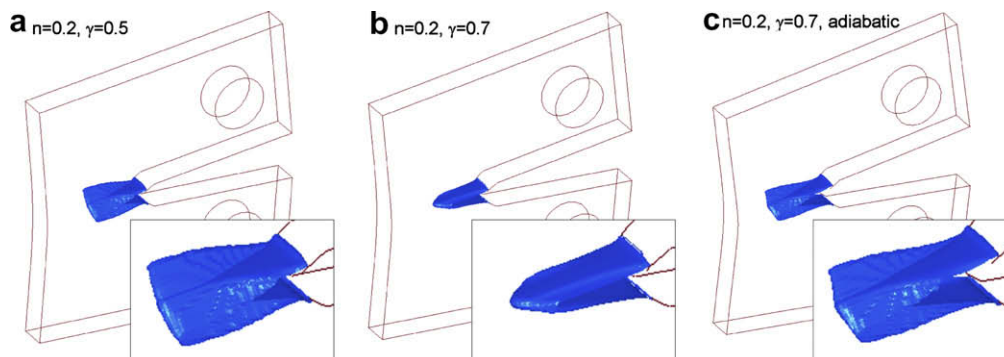

Fig. 3. Crack patterns of compact tension specimens. (a) An overall slant crack ($\gamma = 0.5$) and (b) a flat crack ($\gamma = 0.7$) propagate in the ligaments of compact tension specimens under isothermal condition. (c) Same specimen for ($\gamma = 0.7$) changes to a slant mode under adiabatic loading.
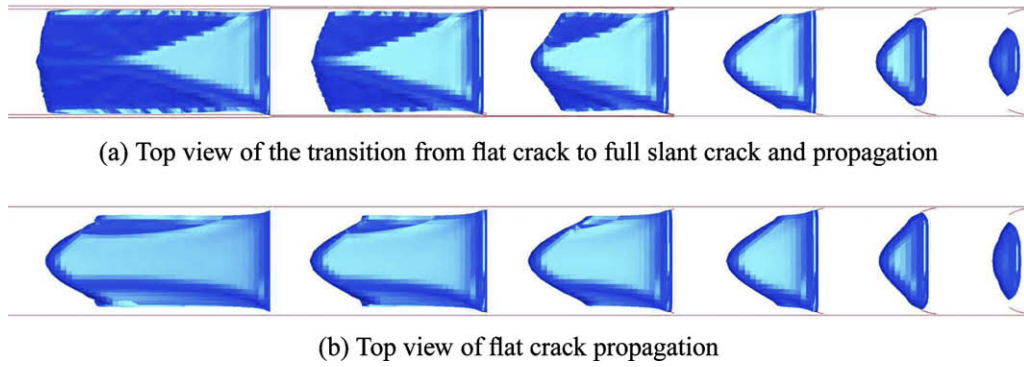
(a) Top view of the transition from flat crack to full slant crack and propagation

(b) Top view of flat crack propagation

Fig. 4. A comparison of crack front evolution: (a) a flat crack becomes a slant crack and (b) a continued flat crack.
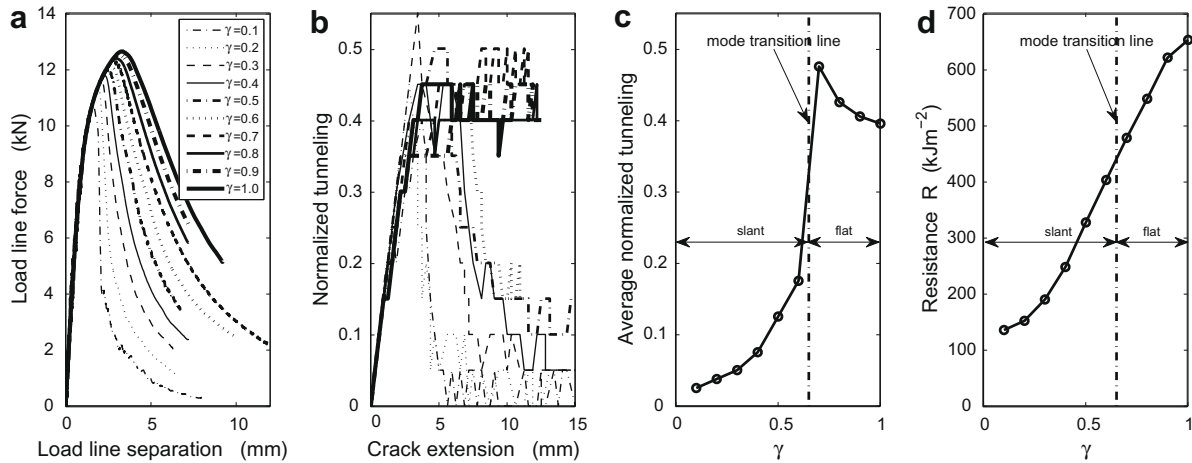

Fig. 5. The load-displacement curves for different γ values (a) and tunnelling (b) and (c). A transition of the tunneling occurs when the global fracture mode changes (b) and (c). However, such mode change has little effect on the trend of the apparent crack growth resistance (d).

(Fig. 5(d)). The apparent crack growth resistance is calculated for the steady crack propagation by integration the load–displacement curve with respect to load line displacement and divided by the cracked ligament area in the original configuration. It is a characteristic of the energy dissipated per unit area of fracture of the material under stable crack advancing. The "apparent fracture area" is obtained by counting the fractured elements in the projection plane perpendicular to the load line. (NOT the fracture surface area, which is about $\sqrt{2}$ times of the "apparent fracture area" for slant crack.) It is shown in Fig. 5(d) that the apparent crack growth resistance grows steadily and no obvious transition in the slope is found at the mode transition line.

Considering the crack advancing, we focus on the damaging and fracturing sequence at the crack tip process zone. A close examination of the stress state reveals two competing damaging mechanisms ahead of the crack tip driven by the mean stress effect and the azimuthal angle effect, respectively. In the three-dimensional fracture envelope shown in Fig. 2, these two mechanisms can be graphically interpreted as (1) the mean stress effect pushing upwards and the fracture envelope shrinks; and (2) the azimuthal angle effect dragging into the "valleys" (where the Lode angle $\theta_L = 0$). In both cases, the damaging process is accelerated at constant plastic strain rate.

The stress state histories of the fractured elements at three different locations – (1) at surface, (2) at 1/4 thickness and (3) at midplane – are plotted in Fig. 6. Several trends emerge from the stress state histories at different locations along crack paths.

Firstly, the azimuthal sensitive factor μ_θ has more contribution in a slant crack, while the pressure sensitive factor μ_p is more important in a flat crack (see the relative position of lines marked by square and triangle in the right subplots, Fig. 6(d) and (h)). In both cases, pressure effect has more influences near the center of the plate – due to the buildup of constraint in the thickness direction. While the damage-averaged stress state sensitive factors μ_θ and μ_p do not vary much in the thickness direction in our calculation, it is noted that the pressure sensitive factor for the slant crack increases sharply near the surface for a slant crack (Fig. 6(d) and (h)). Note a larger sensitivity factor means less influential to damage accumulation. Comparing with a flat crack, the mean stress factor does not change much at the center of the plate for the slant case. The relatively straight crack front and very little necking in the slant mode reduce the constraint in the thickness direction near the surface (see the line marked by square in Fig. 6(d)).

Secondly, the pressure factors (μ_p) increase when the materials approach their final fracture points, which indicate decreasing damage rate. This means the mean stresses decrease before onset of fracture. The reason for this is that the mean stresses reduce as the Young's moduli decrease and, therefore, the initially high mean stresses cannot be hold. In a way, the previous elastic volumetric strain is now generating less mean stress due to a weakened bulk modulus.

Finally, another noticeable feature in the time history of the fractured elements is that there exists a major peak in the azimuthal dependence factor (dash–dot curves in Fig. 6(a)–(c) and (e)–(h)) before the element is fractured and removed. This peak is found for all three locations in the thickness direction for both
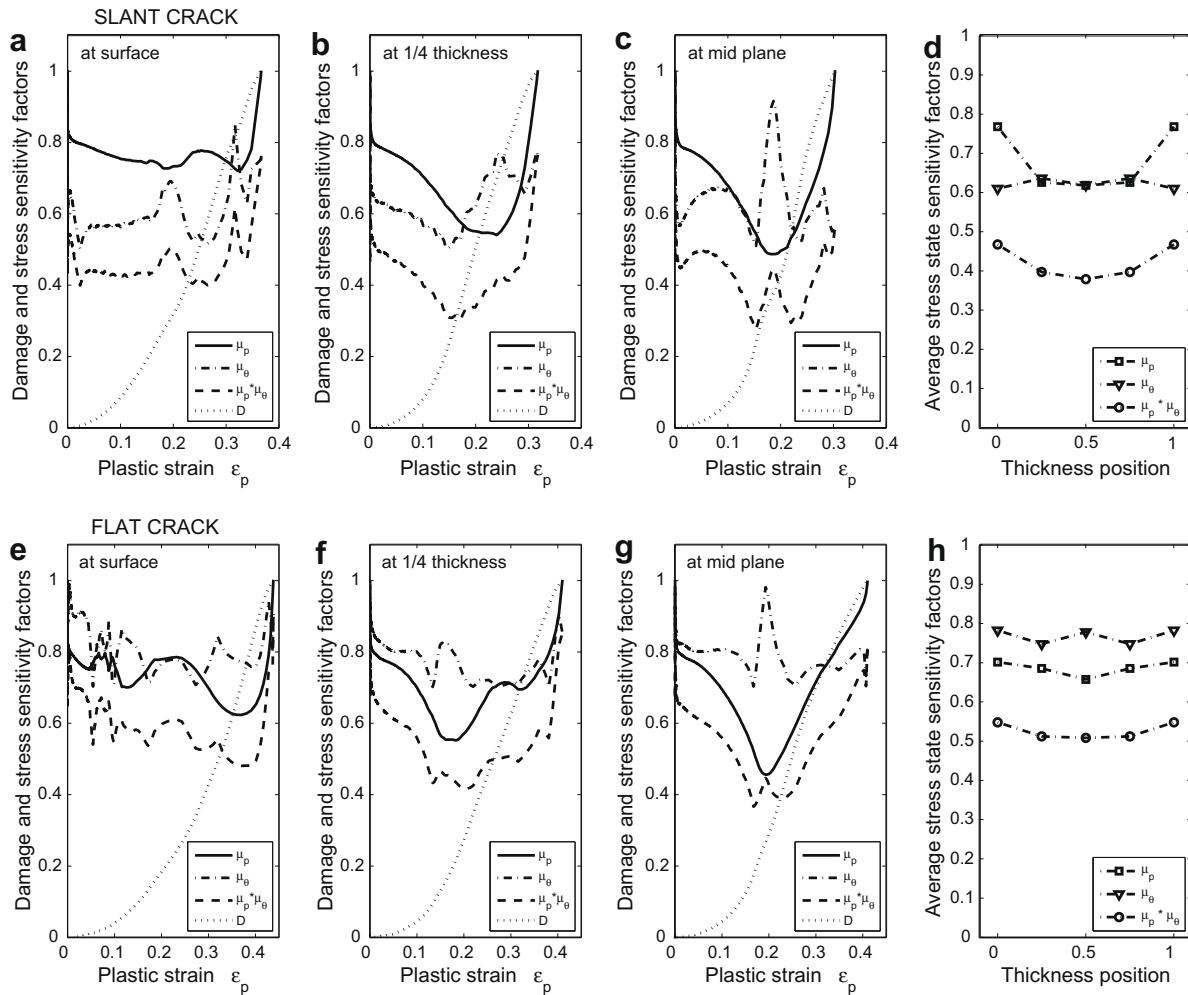
SLANT CRACK

FLAT CRACK

Fig. 6. Time histories of damage (D), pressure sensitivity factor ($\mu_{\rm p}$), azimuthal sensitivity factor (μ_{θ}) and their product at three different locations (a–c; e–g) in the thickness direction for the two fracture modes. The average values of the stress state sensitive factors with respect to damage (d and h) indicate that the governing factors for flat and slant fracture modes are driven by the pressure sensitivity and the Lode angle dependence, respectively.

flat and slant crack modes. An examination in the stress history of the fractured elements shows that this peak is due to the quick buildup of the stress component in the thickness direction (Z), which surpasses the stress component in the crack propagation direction (X), while the stress component in the loading direction (Y) remains the maximum in the fracture process zone. Therefore, the Lode angle of the stress state turns from a close-to-plane-strain condition (a "valley" in the fracture envelope) to a generalized tension condition (a "peak" in a fracture envelope) and then again goes to the other side of the "peak". Thus, a peak is created in the history of the azimuthal dependence factor.

The formation of the shear slips can be illustrated by taking a closer look at the contours of the two competing stress state dependent factors at a cross-section of the flat panel as shown in Fig. 7. The cross-sections are similar to that of the cup-cone fracture of a round bar but the compact tension specimens are more constrained in the propagation direction due to the length of ligament. For a high γ value ($\gamma = 0.7$ as in Fig. 7(a)–(d)), the crack propagation direction is governed by the pressure sensitivity where does not vary much in all directions ahead of the crack tip and dictates the flat crack. On the contrary, for a low γ value ($\gamma = 0.5$ as in Fig. 7(e)–(h)), the crack propagation direction is dictated by the azimuthal dependence factor which forms fast damaging zones at about 45° to the surface (dark areas) and overshadows the pressure dependence factor as shown in Fig. 7(f) and (g).

5. Effect of adiabatic heating

In the dynamic responses of materials, adiabatic heating induces thermal weakening that can trigger shear localization in the heated zone (Bai and Dodd, 1992; Wright and Batra, 1985). The formation of adiabatic shear bands is critical in certain impact and penetration problems. Rivalin et al. (2001) conducted both quasi-static and dynamic experiments on pre-cracked steel plates. In their experiments, a transition from flat quasi-static crack to a slant dynamic crack was found, which suggests the adiabatic behaviour of material can trigger mode transition in dynamic crack propagation. Mathur et al. (1996) analyzed a very thin pre-cracked plate (thickness = 0.33 mm) and showed adiabatic shear banding forms at the slip planes approximately 45° to the surface in a voided media.

For adiabatic loading condition, a classic plasticity work dissipation induced thermal effect is introduced. The yield stress is not generally sensitive to strain rate for aluminum alloys (Zhang and Ravi-Chandar, 2006) and is therefore neglected in the present study. Under the adiabatic condition, the local temperature increase is calculated through the plastic work dissipation, i.e.

$$\rho C_{\rm p} \frac{\partial T}{\partial t} = \alpha \boldsymbol{\sigma} : \mathbf{d}_{\rm p}, \tag{9}$$

where ρ is the material density, $C_{\rm p}$ is the heat capacity, t denotes time, T denotes temperature, $\boldsymbol{\sigma}$ is the stress tensor, $\mathbf{d}_{\rm p}$ is the plastic
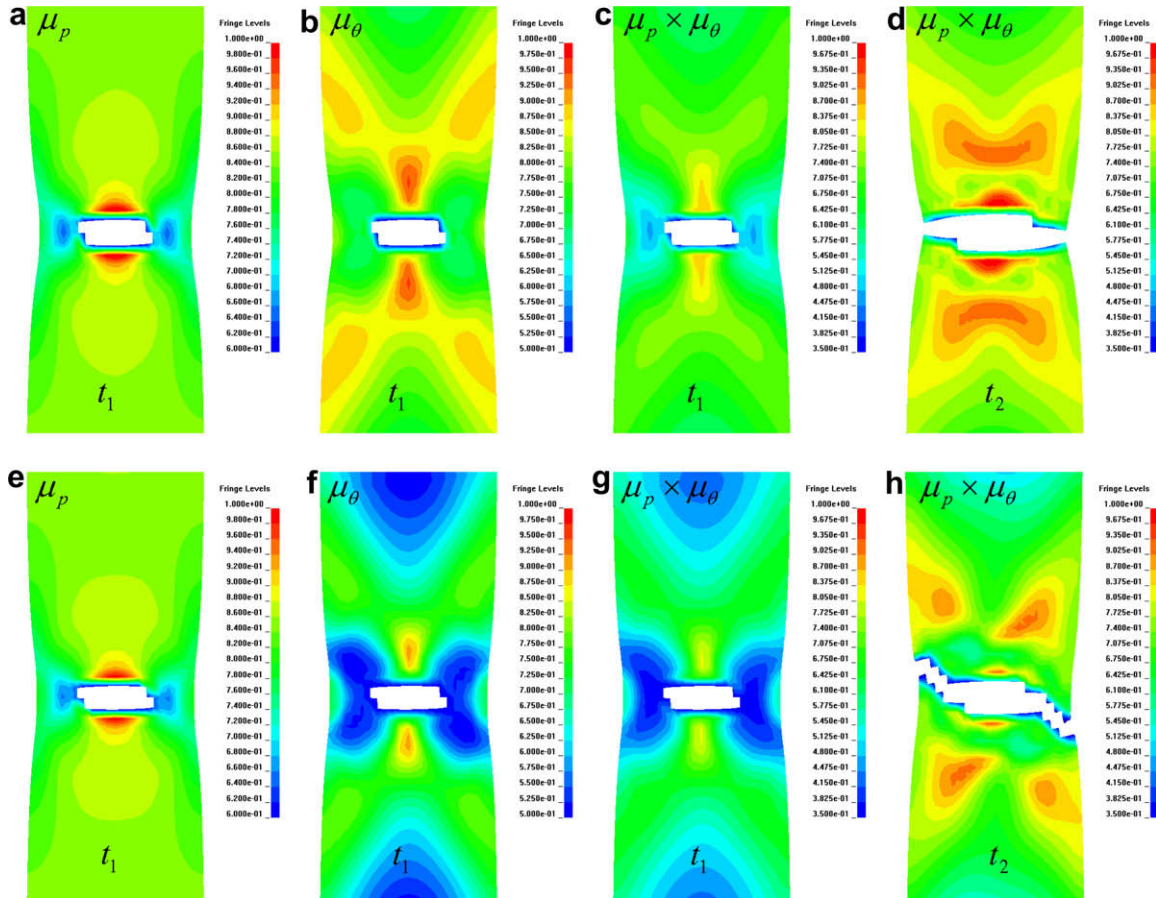
Fig. 7. Contour plots of the pressure sensitivity factor (μ_p), azimuthal sensitivity factor (μ_θ) and their product at a partially cracked cross-section for flat and slant fracture modes. The final through thickness cracks are shown in the right subplots. The azimuthal sensitive factor dictates a slant crack, while the pressure sensitive factor dictates in a flat crack. A smaller sensitivity factor (indicated by dark area) means more influential to the damage accumulation. Panels (a)–(d) are for $\gamma = 0.7$ case and panels (e)–(h) are for $\gamma = 0.5$ case.

part of rate of deformation tensor and α is Taylor–Quinney coefficient, which is taken to be 0.9.

A modified Johnson–Cook thermal weakening factor to the material strength is adopted (Zhang and Ravi-Chandar, 2006). The temperature dependent matrix strength is characterized by

$$\sigma_M = \sigma_{y0}(1 + \varepsilon_p/\varepsilon_0)^n[(T - T_{ref})/(T_{melt} - T_{ref})]^{m_T}, \quad (10)$$

where T is the current temperature of the material, $T_{ref} = 297$ K is a reference temperature (e.g. room temperature where the experiments are conducted), $T_{melt} = 755$ K is the melting temperature for aluminum alloy and the exponent m_T is a material constant, which is chosen to be 1.0 in the present study.

With the thermal weakening, the crack under adiabatic condition turns into a slant crack for $n = 0.2$ and $\gamma = 0.7$ material (Fig. 3(c)), which should be compared with a flat crack for the same material under isothermal condition (Fig. 3(b)). This demonstrates the experimentally observed feature (v).

6. Effect of strain hardening

Experimental results suggest that materials with strong strain hardening capability are more likely to fracture in a flat pattern (Newman, 1985; Pardoen et al., 2004; Pineau and Pardoen, 2007). To further investigate the hardening effect, a series of numerical simulations using the same finite element model is carried out for varying strain hardening exponent n and azimuthal dependence parameter γ to determine the separating line between

the two distinct fracture modes. The results are presented in Fig. 8. The abscissa denotes the azimuthal dependence parameter γ where on the left end $\gamma = 0.0$ means ideal nil ductility in general-
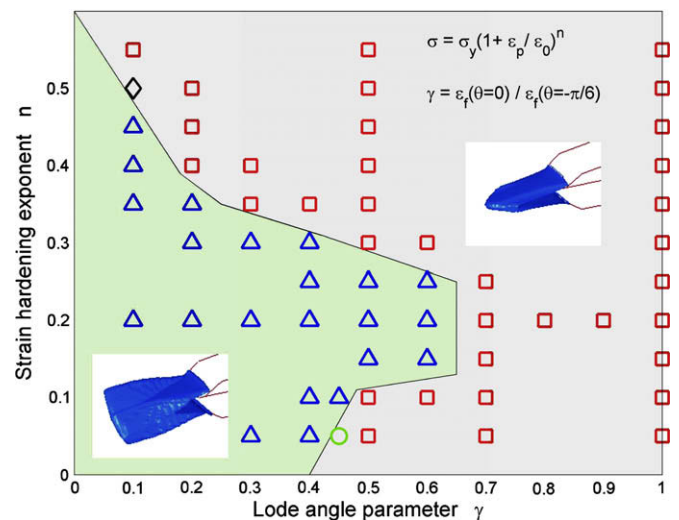

Fig. 8. A fracture mode transition line is determined from a series of numerical simulation results where the strain hardening exponent n and the Lode angle dependence parameter γ are two varying material constants. Triangles denote slant cracks; squares denote flat cracks.
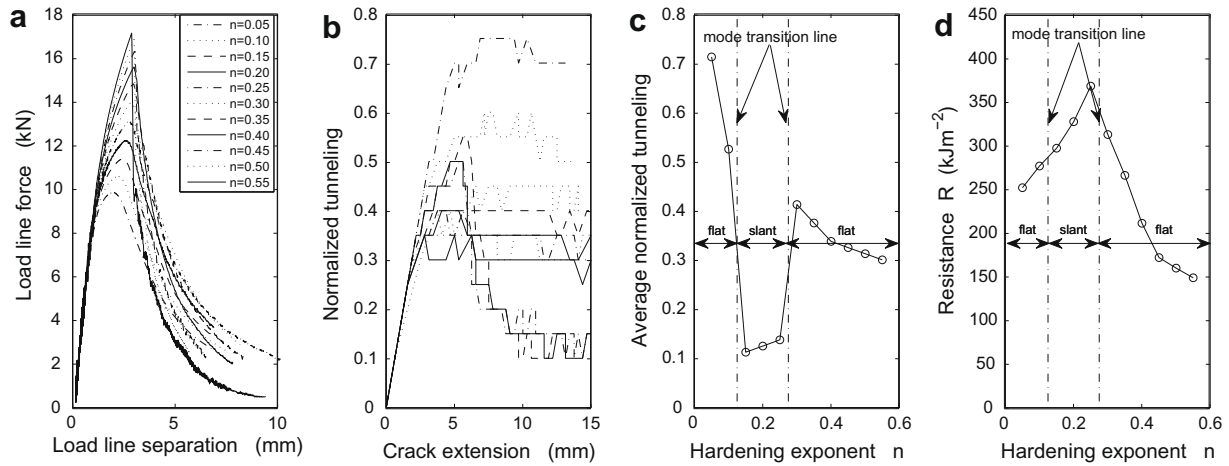
Fig. 9. Fracture characteristics varies with respect to the strain hardening exponent n. Note the distinct normalized tunneling for slant and flat fracture modes for different hardening exponent n. The apparent crack growth resistance increases for small n but decreases for large n.

ized shear condition and on the right end $\gamma = 1.0$ means the fracture envelope is independent of the Lode angle. The coordinate is the strain hardening exponent n which covers a wide range of values for common metals and alloys.

In Fig. 8, near the limiting cases of the transitional boundary, for $n = 0.05$, $\gamma = 0.45$ (circle), the flat crack turned to slant crack after propagates about 10 mm. For $n = 0.50$, $\gamma = 0.10$ (diamond), two tiny shear lips form near free surface and leave a flat zone in the middle; the shear lips never join into a through thickness slant crack.

The results shown in Fig. 8 that the material parameters lead to slant fracture pattern locate at the low left corner of the $\gamma - n$ matrix (indicated by a light green color[1]). The remaining regime where a flat crack is found is shown in grey color. A transitional boundary is also shown in Fig. 8 as a solid line. Above the boundary line, the strain hardening exponent is large and the mean stress influence is significant in the flat panel, which leads to a flat crack. This agrees the well-known experimental observations, i.e. experimentally observed feature (i).

Another pattern emerges from Fig. 8 is that low Lode angle dependence (i.e. larger γ values) tends to result in a flat crack. This can be seen from the right-hand side of the boundary, the Lode angle dependence of fracture is diminishing and a flat crack is observed. However, this effect is not known previously due to the inadequate awareness of the azimuthal dependence of ductile fracture in the literature. Further experimental verification is in need in this regard.

Similar to Fig. 5, we draw conclusions from Figs. 9 and 10 on the dependence of fracture characteristics with respect to the strain hardening exponent n (for fixed $\gamma = 0.5$ and $q = 1.0$) and the pressure sensitivity parameter q (for fixed $\gamma = 0.5$ and $n = 0.2$). In Figs. 9 and 10, slant cracks are found in the intermediate range of n and q values. For small n, the deformation is highly localized in the crack plane. When constraints are build-up in the thickness direction, significant tunneling propagates in the mid-plane (Fig. 9(c)), which is followed by lateral propagation instead of forming shear lips at the tail of the crack. For large n, excessive pressure build-up drives the material to fracture in a flat pattern. It should be noted that the fracture transition between intermediate and large values of n, the crack growth resistance peaked and then drops when $n > 0.25$ (Fig. 9(d)).

For small q, because of the diminishing pressure sensitivity, excessive necks form ahead of the crack tip and result in an overall flat crack in the significantly reduced section thickness due to geometrical influence. In this case, the influence of geometrical change in the fracture process zone is significant. The plastic strain rate (in Eq. (2)) in the normal section is much greater than the rest. For large q, the material is highly sensitive to pressure and breaks in cleavage manner. This can be seen from Fig. 9(d) that the crack growth resistance drops to almost zero for $q > 2.0$.

From the vertical line of $\gamma = 1$ in Fig. 5, without the consideration of the Lode angle dependence of ductile materials, the predicted fracture modes are all flat cracks. Because of this reason, all numerical studies published in the literature have not been able to predict a slant crack and to capture the five distinctive features listed in Section 1. As for the formation of shear lips, Tvergaard and Needleman (1984) simulated the flat-to-slant transition in the cup-cone rupture of round bars using micromechanical modified Gurson model (Gurson, 1977) and explained the formation of shear lips near surface due to "void sheeting mechanism" of secondary particles. The cup-cone transition can also be found in numerical simulations using continuum damage mechanics (Teng, 2008 etc.). However, the modified Gurson model and the conventional continuum damage mechanics method do not include the effect of third stress invariant (in other word, $\gamma = 1.0$ is tacitly assumed). From Fig. 8, under the present assumptions, a slant crack in thin plate cannot be predicted without introducing additional effects, such as adiabatic heating (Mathur et al., 1996) or anisotropy (Besson et al., 2001). Further modifications to the Gurson-type models are also introduced by Xue (2006) to include damages associated with void shearing that is dependent on the Lode angle (Xue, 2007b, 2008). Similar remedy was adopted by Nahshon and Hutchinson (2008) to include a third stress invariant dependent damage evolution law more recently.

7. Effect of plate thickness

The general opinion about crack growth resistance for flat plates is that it increases at low thickness where a slant crack is observed and decreases with respect to thickness as mode I crack becomes dominant. Eventually, the crack growth resistance reaches its asymptotic value of the mode I fracture for very thick plate. This phenomenon is well known to the experimentalists when measuring the fracture toughness for ductile materials using flat plates of
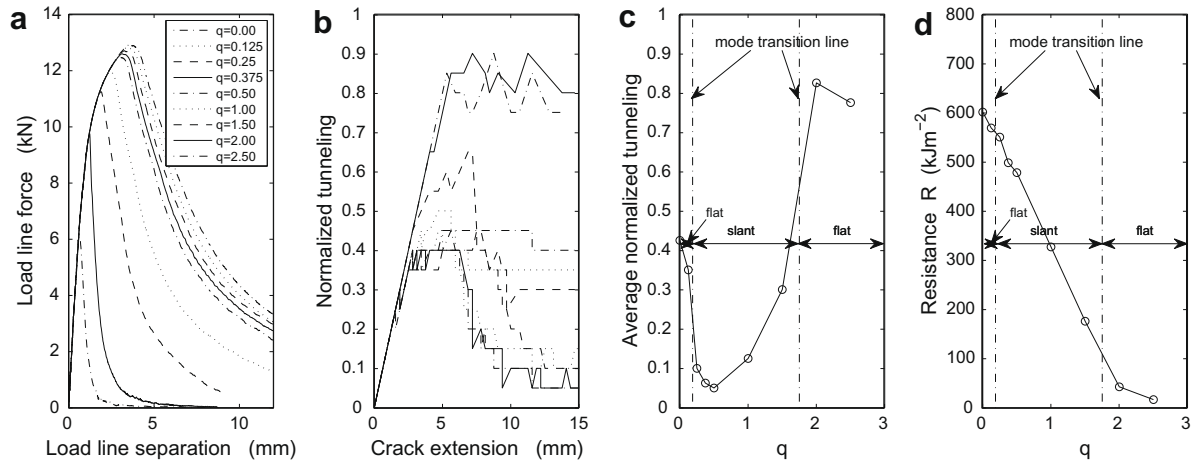
---

[1] For interpretation of the references to color in Fig. 8, the reader is referred to the web version of this paper.

Fig. 10. Fracture characteristic varies with respect to the pressure sensitivity parameter q. The apparent crack growth resistance decreases with increasing pressure sensitivity (increasing q values). The fracture mode does not have an obvious effect on R value (d), but slant crack significantly reduces the tunneling effect (c).

different thicknesses (Broek, 1982, Chapter 4; Barsom and Rolfe, 1999, Chapter 4; Anderson, 2005, Chapter 2).

A phenomenological explanation is given by Krafft et al. (1961) who separated the energy dissipation of the shear lips (slant region) from the grossly flat central zone in fractured thick plates. They explained the increase of crack growth resistance in the small thickness regime is due to the energy dissipation in a quadratic form to the depth of shear lip and in the large thickness regime the depth of shear lips is bounded and eventually only energy associated with mode I is dissipated. We simulate the fracture of compact tension specimens for various thicknesses and the crack growth resistances are calculated.

Simulations are performed for a series of compact tension plates for $n = 0.2$, $\gamma = 0.5$ and with thickness various from 1.5875 to 25.4 mm. The 1.5875 mm thick plate buckles in the ligament and therefore is excluded from the following discussion. The results are shown in Fig. 11. From Fig. 11, the center portion of the crack surface becomes flat as the thickness of the plates increases. For thinner plates (thickness equals 6.35 mm and less), an overall slant mode is observed throughout the thickness. For thicker plates (greater than 6.35 mm), the specimens show (1) a central flat zone where materials fail in mode I opening mode and (2) two shear lip zones where mixed I/III mode slant cracks form. Due to the differences in fracture mechanisms of the flat and slant regimes, the apparent crack propagation resistance varies with the plate thickness. The apparent crack growth resistance is computed from the

crack surface in the original configuration projected to the initial crack plane. The trend obtained from the numerical simulation represents the well-known shape of thickness dependence curve of the crack growth resistance, as shown in Fig. 12(d). The maximum thickness calculated here is 25.4 mm, which is limited to the excessive computational time. It appears that the plane strain limit has not been reached yet for this hypothetical material.

It is also noticed that the apparent crack growth resistance R does not decrease immediately after the appearance of a flat region at the center of the fracture surface. Rather, the apparent crack growth resistance continues to increase until thickness reaches about 10 mm when the flat region consists of about 20% of the thickness. The flat portion of in the thickness direction increases with increasing thickness as shown in Fig. 12. This matches the experimental observation feature (iv).

8. Mesh size dependence

In the late stage of deformation of an element, the hardening modulus of the material becomes non-positive when damage becomes important. The numerical solution is mesh sensitive as this type of damage constitutive relationships usually do. One way to regulate the deformation is to include a characteristic length scale in the constitutive model or a strain gradient dependent term in the damaging process. The present damage plasticity model does not incorporate such an inherent length scale, therefore, the solu-
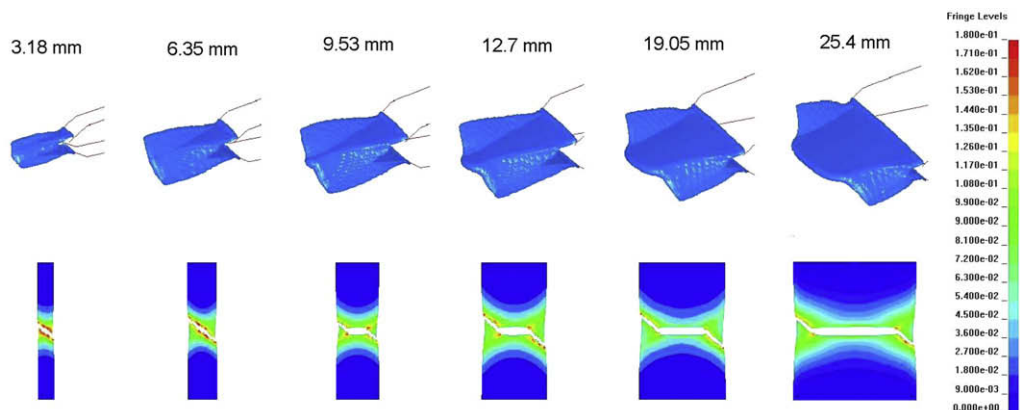

Fig. 11. The appearance of crack surface varies with the plate thickness. With increasing plate thickness, the flat zone initiates at the center and grows.
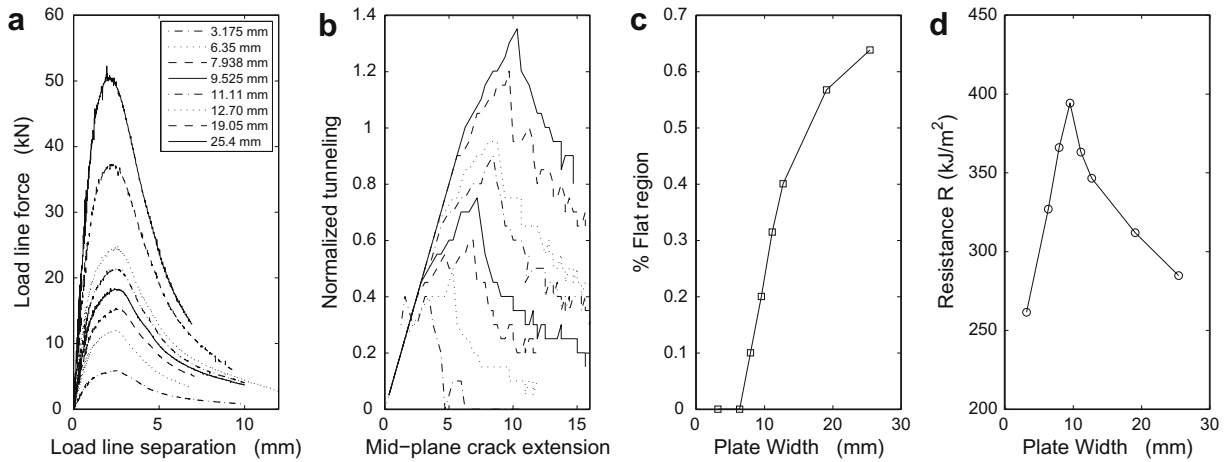
Fig. 12. The load-displacement curves (a) and the relationships between the tunneling (b), the percentage of the flat portion of the crack surface (c), the apparent crack growth resistance (d) and the plate thickness are plotted for the simulation results. The flat portion of the fracture surface increases with increasing plate thickness. The apparent crack growth resistance peaked at about 10 mm plate thickness.

tion is mesh dependent. Moreover, the slant mode of fracture is usually localized in narrow shear bands. The characterization of these shear bands certainly relies on the size of the mesh. Coarse mesh may not be able to depict the details in a shear band and lead to a different fracture mode (in the present study, a flat mode is found instead for coarse meshes).

A series of numerical simulations were conducted to further investigate the dependence of mode transition on the mesh size. The 6.35-mm-thick compact tension specimen is discretized by different size of elements. We denote the element size by the number of elements in the thickness direction of the plate. The number of elements in the thickness direction varies from 5 to 25 elements (element size 1.27–0.254 mm). The aspect ratio of the elements along and in the neighborhood of the crack path is kept 1:1:1.

The matrix stress–strain curve remains the same as the base scenario, where the hardening exponent $n = 0.2$. The pressure dependence parameters are the same. We also explore the dependence of the mode transition on the Lode angle dependence parameter γ, which has been identified as one of the key parameters for the mode transition in flat plate. The results with respect to
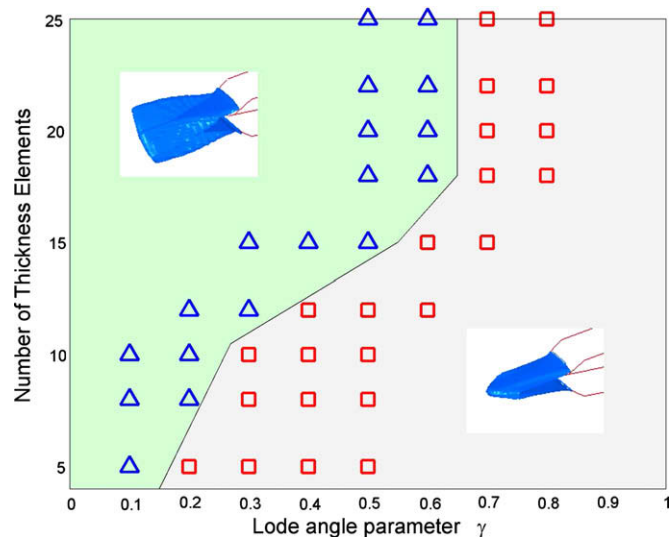
the element size and the Lode angle dependence are plotted in Fig. 13.

From Fig. 13, smaller element size are more capable of capturing a slant mode of fracture for a fixed γ. There appears a transition line between the flat and the slant modes of fracture. The transition line is plotted in Fig. 13 as a thin solid line. The simulations where a slant mode is found are indicated by a triangle and where a flat mode is found are indicated by a square. The critical number of elements in the thickness direction to capture a slant mode depends on the tendency of the material on how easy a shear band forms. For instance, at low γ values (e.g. $\gamma \in [0.1, 0.2]$), less than 10 elements are need to capture a slant mode (element size 0.635 mm). At higher values, e.g. $\gamma = 0.5$, 15 elements are needed (element size 0.423 mm). For the number of through thickness element greater than 18, the slant mode of failure persists for all γ values when other material parameters are fixed.

Nine load–displacement curves for different mesh sizes of the same compact tension specimen and same material parameters are plotted in Fig. 14. For the same set of material parameters, the load–displacement curve drops when the mesh is finer. The crack pattern and energy dissipation when crack propagates appear to be sensitive to the mesh size. At low resolution of discretization (the number of through thickness elements between 5 and 12), the numerical results show a flat crack, which indicates the shear bands in the thickness direction cannot be captured. The significance of the tunneling effect becomes more obvious when the mesh size decrease (see Fig. 14(b) and (c)). When the number of through thickness elements is equal or greater than 15, the resolution of the mesh becomes capable of depicting the shear bands. In these simulations, shear lips form first and then the entire crack front changes to a slant pattern after a short transitional area. Due to the diminishing constraint in the thickness direction for a slant crack, the tunneling effect also decreases when the mesh becomes finer.

The apparent crack growth resistance is a monotonic decreasing function with the number of elements in the thickness direction. When elements become smaller, the crack processing zone is characterized in more details. The deformation is more localized in the shear bands such that the energy dissipation is narrowed to a smaller zone. This yields the continuous decreasing of the apparent crack growth resistance with finer mesh. It also appears that the mode of crack does not have an obvious impact on the apparent crack resistance. The transition line between the two modes depending on the mesh size is marked in Fig. 14(c) and (d).

Fig. 13. The numerical results of fracture mode depend on the mesh size and the Lode angle dependence factor γ. For example, the critical number of elements in the thickness direction is 15 for $\gamma = 0.5$ to capture a slant mode in this case (element size 0.423 mm).
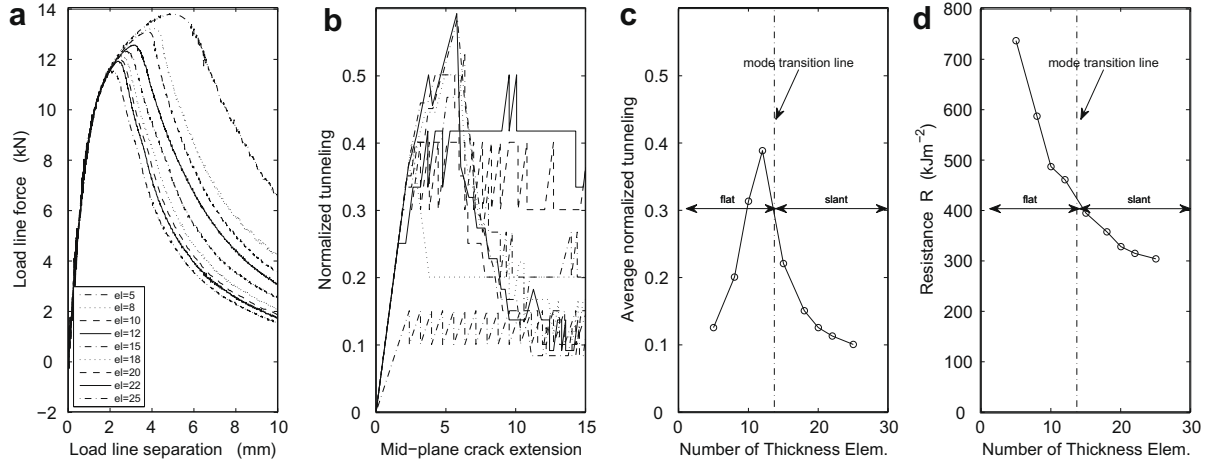
Fig. 14. The load-displacement curves (a) and the relationships between the tunneling (b) and (c), the apparent crack growth resistance (d) and the number of through thickness elements are plotted for the simulation results.

9. Conclusions

We have determined that the crack mode in ductile flat panels is governed by the interaction of the pressure sensitivity and the Lode angle dependence characteristics of the material. The Lode angle dependence was a missing ingredient in the constitutive characterization of the ductility of material in existing theories. By including this additional dimension, the underlying competing fracture mechanisms are revealed. The novelty of this work also resides in the systematic investigation of the influencing factors of the strain hardening, the Lode angle parameter and the hydrostatic pressure parameter on the ductile fracture characteristics that was not fully explored and addressed in the literature. Experimentally observed distinct fracture modes are reproduced by a series of finite element simulations. It is remarkable that all major features of the dependence of mode transition upon the material hardening capacity, the Lode angle dependence parameters, the tunneling effect, the adiabatic heating induced mode transition and the thickness dependence of apparent crack growth resistance are captured using the newly developed continuum theory of damage plasticity.

Also investigated in the present research is the mesh size dependence of ductile fracture. It is well known that the numerical solution of this type of damage model without an inherent length scale is mesh size dependent when fracture is concerned. In the compact tension case, the shear bands cannot be correctly repre-

sented when the resolution of the mesh is low. A series of simulations for different mesh sizes and the Lode angle dependence parameters γ is conducted. A flat crack is observed for relatively coarse mesh and a slant crack is observed for finer mesh when the geometry and the material constants remain the same. The apparent crack growth resistance is found to decrease with decreasing element size.

Further elucidation of the local damaging process at the crack tip requires higher resolution in the dependence functions on the mean stress and the azimuthal angle, the damage evolution law and the damage-coupled yield function. Given the state-of-art experimental technique, the determination of these functions remains difficult. We envision a continued progress in describing and predicting ductile fracture under the proposed framework.

Appendix A

For illustration purpose, the evolution of the deviatoric stress tensor is graphically represented in Fig. 15 for the one-dimensional case, where the deviatoric stress goes from s_n at time t_n to s_{n+1} at time t_{n+1} with weakening considered. The abscissa is the total strain.

An explicit stress integration procedure is used in the calculation in the present study. At time t_n, two state variables, ε_n^p and D_n and the stress state σ_n are given[2]. The stress integration procedure is the following:

Given: $\{\sigma_n, \varepsilon_n^p, D_n\}$ and $\Delta\varepsilon = \varepsilon_{n+1} - \varepsilon_n$ at time t_n.
Step 1:
Calculate

$$\left.\begin{aligned}
\varepsilon_n^e &= \frac{1}{w(D_n)}\mathbb{C}_0^{-1} : \sigma_n; \\
\varepsilon^\dagger &= \varepsilon_n^e + \Delta\varepsilon; \\
\hat{\varepsilon} &= \varepsilon^\dagger - \frac{1}{3}(\mathrm{tr}\varepsilon^\dagger)\mathbf{1}; \\
\tilde{\varepsilon} &= \sqrt{\frac{2}{3}\hat{\varepsilon} : \hat{\varepsilon}},
\end{aligned}\right\} \tag{11}$$

$$\sigma_{n+1}^{\mathrm{trial}} = \sigma_n + w(D_n)\mathbb{C}_0 : [\Delta\varepsilon], \tag{12}$$
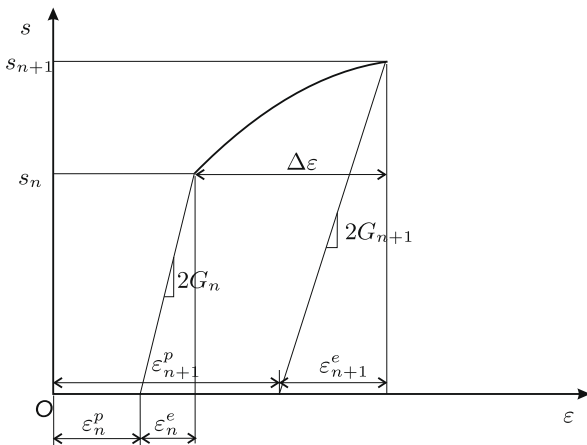

Fig. 15. A schematic drawing illustrates the evolution of the deviatoric stress tensor for the one-dimensional case.

---

[2] Bold faced letters are tensors.

where $\mathbb{C}_0$ is the fourth order ground-state isotropic elasticity tensor, i.e.

$$\mathbb{C}_0 = 2G_0\mathbb{I} + \left(K_0 - \frac{2}{3}G_0\right)\mathbf{1} \otimes \mathbf{1}, \tag{13}$$

where $\mathbb{I}$ is the fourth order identity tensor and $\mathbf{1}$ is the second order identity tensor.

$$\sigma_{\text{eq}}^{\text{trial}} = 3w(D_n)G_0\tilde{\varepsilon}. \tag{14}$$

Step 2:
IF

$$\sigma_{\text{eq}}^{\text{trial}} \leqslant (1 - D_n)\sigma_{\text{M}n}(\varepsilon_n^p). \tag{15}$$

THEN (*elastic update*)

$$\left.\begin{aligned}\boldsymbol{\sigma}_{n+1} &= \boldsymbol{\sigma}_{n+1}^{\text{trial}}; \\ \varepsilon_{n+1}^p &= \varepsilon_n^p; \\ D_{n+1} &= D_n.\end{aligned}\right\} \tag{16}$$

ELSE IF

$$\sigma_{\text{eq}}^{\text{trial}} > (1 - D_n)\sigma_{\text{M}n}(\varepsilon_n^p), \tag{17}$$

THEN (*elastic–plastic update*)

$$\left.\begin{aligned}\mathbf{n}_{n+1} &= \frac{3}{2}\frac{\mathbf{s}^{\text{trial}}}{\sigma_{\text{eq}}^{\text{trial}}}; \\ \Delta\varepsilon^p &= \frac{3G_0\tilde{e} - \sigma_{\text{M}n}}{3G_0 + h}; \\ \Delta\boldsymbol{\varepsilon}^p &= \Delta\varepsilon^p\mathbf{n}_{n+1},\end{aligned}\right\} \tag{18}$$

and

$$\left.\begin{aligned}\mu_{\text{p}} &= \begin{cases}1 - q\log\left(1 - \frac{p}{p_{\text{lim}}}\right), & p \geqslant p_{\text{lim}}[1 - \exp(1/q)]; \\ 0, & p < p_{\text{lim}}[1 - \exp(1/q)],\end{cases} \\ \mu_{\theta} &= \gamma + (1 - \gamma)\left(\frac{6|\theta_{\text{L}}|}{\pi}\right)^k; \\ \varepsilon_{\text{f}} &= \varepsilon_{\text{f}0}\mu_{\text{p}}\mu_{\theta},\end{aligned}\right\} \tag{19}$$

and

$$\left.\begin{aligned}D_{n+1} &= D_n + m\left(\frac{\varepsilon_n^p}{\varepsilon_{\text{f}}}\right)^{(m-1)}\frac{\Delta\varepsilon^p}{\varepsilon_{\text{f}}}; \\ w(D_{n+1}) &= 1 - D_{n+1}^{\beta}; \\ \varepsilon_{n+1}^p &= \varepsilon_n^p + \Delta\varepsilon^p,\end{aligned}\right\} \tag{20}$$

and

$$\left.\begin{aligned}\boldsymbol{\varepsilon}_{n+1}^e &= \boldsymbol{\varepsilon}^{\dagger} - \Delta\boldsymbol{\varepsilon}^p; \\ \boldsymbol{\sigma}_{n+1} &= w(D_{n+1})\mathbb{C}_0\boldsymbol{\varepsilon}_{n+1}^e.\end{aligned}\right\} \tag{21}$$

END

All necessary field variables $\{\boldsymbol{\sigma}_{n+1}, \varepsilon_{n+1}^p, D_{n+1}\}$ are updated at time $t_{n+1} = t_n + \Delta t$.

References

Anderson, T.L., 2005. Fracture Mechanics: Fundamentals and Applications, third ed. CRC Press, Boca Raton, FL.

Arun Roy, Y., Dodds Jr., R.H., 2001. Simulation of ductile crack growth in thin aluminum panels using 3-D surface cohesive elements. International Journal of Fracture 110, 21–45.

Bai, Y., Dodd, B., 1992. Adiabatic Shear Localization. Pergamon Press, Oxford.

Bao, Y., Wierzbicki, T., 2004. On fracture locus in the equivalent strain and stress triaxiality space. International Journal of Mechanical Sciences 46, 81–98.

Barsom, J.M., Rolfe, S.T., 1999. Fracture and Fatigue Control in Structures – Applications of Fracture Mechanics, third ed. Butterworth–Heinemann, Woburn, MA.

Barsoum, I., Faleskog, J., 2007. Rupture mechanisms in combined tension and shear – experiments. International Journal of Solids and Structures 44, 1768–1786.

Benzerga, A.A., Besson, J., Pineau, A., 2004. Anisotropic ductile fracture. Part I: experiments. Acta Materialia 52 (15), 4623–4638.

Besson, J., Brocks, W., Chabanet, O., Steglich, D., 2001. Ductile rupture of aluminium sheet materials. In: Saanouni, K. (Ed.), Numerical Modelling in Damage Mechanics (NUMEDAM'00), Revue Européenne des Éléments Finis, vol. 10, pp. 401–415 (from Chabanet, O. et al., 2003, Predicting crack growth resistance of aluminium sheets, Comput. Mater. Sci. 26, 1–12.).

Bridgman, P.W., 1952. Studies in Large Plastic Flow and Fracture. McGraw-Hill, New York.

Broek, D., 1982. Elementary Engineering Fracture Mechanics, third ed. Sijthoff & Noordhoff, Alphena.

Clausing, D.P., 1970. Effect of plastic strain state on ductility and toughness. International Journal of Fracture Mechanics 6 (1), 71–85.

Cottrell, A.H., 1965. Mechanics of fracture in large structures. Proceedings of the Royal Society of London Series A: Mathematical and Physical Sciences 285 (1400), 10–21.

Dawicke, D.S., Sutton, M.A., 1994. CTOA and crack tunneling measurements in thin sheet 2024-T3 aluminum alloy. Experimental Mechanics 34, 357–368.

Dawicke, D.S., Newman Jr., J.C., Bigelow, C.A., 1995. Three-dimensional CTOA and constraint effects during stable tearing in a thin-steel material. Fracture Mechanics: ASTM STP 1256 26, 223–242.

Gao, X., Wang, T., Kim, J., 2006. On ductile fracture initiation toughness: effects of void volume fraction, void shape and void distribution. International Journal of Solids and Structures 43, 6165–6179.

Gullerud, A.S., Dodds Jr., R.H., Hampton, R.W., Dawicke, D.S., 1999. Three-dimensional modeling of ductile crack growth in thin sheet metals: computational aspects and validation. Engineering Fracture Mechanics 63, 347–374.

Gurson, A.L., 1977. Continuum theory of ductile rupture by void nucleation and growth. Part I. Yield criteria and flow rules for porous ductile media. Journal of Engineering Materials and Technology – Transactions of ASME 99, 2–15.

Hutchinson, J.W., 1968. Singular behaviour at the end of a tensile crack in a hardening material. Journal of the Mechanics and Physics of Solids 16, 13–31.

Irwin, G.R., Kies, J.A., Smith, H.L., 1958. Fracture strengths relative to onset and arrest of crack propagation. In: Proceedings of the ASTM, vol. 58, ASTM, Philadelphia, PA.

James, M.A., Newman Jr., J.C., 2003. The effect of crack tunneling on crack growth: experiments and CTOA analysis. Engineering Fracture Mechanics 70, 457–468.

Kim, J., Zhang, G., Gao, X., 2007. Modeling of ductile fracture: application of the mechanism-based concepts. International Journal of Solids and Structures 44, 1844–1862.

Knott, J.F., 1973. Fundamentals of Fracture Mechanics. Butterworths, London.

Krafft, J.M., Sullivan, A.M., Boyle, R.W., 1961. Effect of dimensions on fast fracture instability of notched sheets. In: Proceedings of Crack Propagation Symposium, vol. 1, College of Aeronautics, Cranfield, England, pp. 8–12.

Lan, W., Deng, X., Sutton, M.A., Cheng, C.S., 2006. Study of slant fracture in ductile materials. International Journal of Fracture 141, 469–496.

Li, S., Liu, W.K., Rosakis, A.J., Belytschko, T., Hao, W., 2002. Mesh-free Galerkin simulations of dynamic shear band propagation and failure mode transition. International Journal of Solids and Structures 39, 1213–1240.

Mahmoud, S., Lease, K., 2003. The effect of specimen thickness on the experimental characterization of critical crack-tip-opening angle in 2024-T351 aluminum alloy. Engineering Fracture Mechanics 70, 443–456.

Mahmoud, S., Lease, K., 2004. Two-dimensional and three-dimensional finite element analysis of critical crack-tip-opening angle in 2024-T351 aluminum alloy at four thickness. Engineering Fracture Mechanics 71, 1379–1391.

Mathur, K.K., Needleman, A., Tvergaard, V., 1996. Three-dimensional analysis of dynamic ductile crack growth in a thin plate. Journal of the Mechanics and Physics of Solids 44 (3), 439–464.

McClintock, F.A., 1971. Plasticity aspects of fracture. Fracture An Advanced Treatise, vol. III. Academic Press, New York. pp. 47–307 (Chapter 2).

Nahshon, K., Hutchinson, J.W., 2008. Modification of the Gurson model for shear failure. European Journal of Mechanics A/Solids 27, 1–17.

Newman Jr., J.C., 1985. An evaluation of fracture analysis methods. In: Newman, J.C., Jr., Loss, F.J. (Eds.), Elastic–Plastic Fracture Mechanics Technology, ASTM STP 896. ASTM, Philadelphia, PA.

Newman Jr., J.C., James, M.A., Zerbst, U., 2003. A review of the CTOA/CTOD fracture criterion. Engineering Fracture Mechanics 70, 371–385.

Pardoen, T., Hachez, F., Marchioni, B., Blyth, P.H., Atkins, A.G., 2004. Mode I fracture of sheet metal. Journal of the Mechanics and Physics of Solids 52, 423–452.

Pineau, A., Pardoen, T., 2007. Failure mechanisms of metals. Comprehensive Structural Integrity Encyclopedia. Failure Mechanisms of Metals, vol. 2. Elsevier, Amsterdam (Chapter 6).

Pugh, H.Ll.D., 1970. Mechanical behavior of materials under pressure. The Application of Hydrostatic Pressure to the Forming of Metals. Elsevier, Amsterdam. pp. 522–590 (Chapter 10).

Rice, J.R., Rosengren, G.F., 1968. Plane strain deformation near a crack tip in a power-law hardening material. Journal of the Mechanics and Physics of Solids 16, 1–12.

Rivalin, F., Pineau, A., Di Fant, M., Besson, J., 2001. Ductile tearing of pipeline-steel wide plates I: dynamic and quasi-static experiments. Engineering Fracture Mechanics 68, 329–345.

Srawley, J.E., Brown Jr., W.F., 1965. Fracture toughness testing. Technical Report NASA-TN-D-2599, NASA, Washington, DC.

Teng, X., 2008. Numerical prediction of slant next term fracture with continuum damage mechanics. Engineering Fracture Mechanics 75 (8), 2020–2041.

Thomason, P.F., 1990. Ductile Fracture of Metals. Pergamon Press, Oxford.

Tvergaard, V., Needleman, A., 1984. Analysis of the cup-cone fracture in a round tensile bar. Acta Metallurgica 32 (1), 157–169.

Tvergaard, V., Needleman, A., 2006. Three dimensional microstructural effects on plane strain ductile crack growth. International Journal of Solids Structures 43, 6165–6179.

Wilkins, M.L., Streit, R.D., Reaugh, J.E., 1980. Cumulative-strain-damage model of ductile fracture: simulation and prediction of engineering fracture tests, Technical Report UCRL-53058, Lawrence Livermore National Laboratory.

Wright, T.W., Batra, R.C., 1985. The initiation and growth of adiabatic shear bands. International Journal of Plasticity 1 (3), 205–212.

Xia, L., Shih, C.F., Hutchinson, J.W., 1995. A computational approach to ductile crack growth under large scale yielding conditions. Journal of the Mechanics and Physics of Solids 43 (3), 389–413.

Xue, L., 2006. Void shearing effect in ductile fracture of porous materials. In: Besson, J. et al. (Eds.), Local Approach to Fracture, Proceedings of the 9th European Mechanics of Materials Conference, pp. 483–488.

Xue, L., 2007a. Damage accumulation and fracture initiation of uncracked ductile solids subjected to triaxial loading. International Journal of Solids and Structures 44, 5163–5181.

Xue, L., 2007b. Ductile fracture modeling – theory, experimental investigation and numerical verification, Ph.D. Dissertation, Massachusetts Institute of Technology.

Xue, L., 2008. Constitutive modeling of void shearing effect in ductile fracture of porous materials. Engineering Fracture Mechanics 75 (11), 3343–3366.

Xue, L., Wierzbicki, T., 2008. Ductile fracture initiation and propagation modeling using damage plasticity theory. Engineering Fracture Mechanics 75 (11), 3276–3293.

Xue, L., Wierzbicki, T., submitted for publication. Ductile fracture characterization of aluminum alloy 2024-T351 using damage plasticity theory.

Zhang, H., Ravi-Chandar, K., 2006. On the dynamics of necking and fragmentation. I. Real-time and post-mortem observations in Al 6061-O. International Journal of Fracture 142, 183–217.